Simulation of L-Band Bistatic Returns From the Ocean Surface: A Facet Approach With Application to Ocean GNSS Reflectometry

Maria Paola Clarizia, *Student Member, IEEE*, Christine Gommenginger, Maurizio Di Bisceglie, *Member, IEEE*, Carmela Galdi, *Member, IEEE*, and Meric A. Srokosz

***Abstract*—We present the implementation of a facet-based simulator to investigate the forward scattering of L-band signals from realistic sea surfaces and its application to spaceborne ocean Global Navigation Satellite System (GNSS) Reflectometry. This approach provides a new flexible tool to assess the influence of the ocean surface roughness on scattered GNSS signals. The motivation stems from the study by Clarizia *et al.*, which revealed significant differences between delay–Doppler maps (DDMs) obtained from UK-DMC satellite data and DDMs simulated with the Zavorotny–Voronovich (Z-V) model. Here, the scattered power and polarization ratio (PR) are computed for explicit 3-D ocean wave fields, using a novel implementation of the Kirchhoff approximation (KA), which we call the Facet Approach (FA). We find that the FA is consistent with the full KA and the Geometrical Optics (GO) used in the Z-V model, while being less computationally expensive than the KA and able to represent polarization effects not captured by the GO. Instantaneous maps of the bistatic normalized radar cross section computed with the FA show clear patterns associated with the underlying waves. The wave field is particularly visible in the PR, indicating that the scattering is generally dominated by the HH component, particularly from ocean wave troughs. Polarization effects show, for the first time, a strong correlation to the explicit sea surface from which the scattering originated. DDMs of the scattered power computed with the FA reveal patchy patterns and power distributions that differ from those obtained with Z-V and show closer similarities with observed DDMs from UK-DMC.**

***Index Terms*—Facet approach (FA), Global Navigation Satellite System Reflectometry (GNSS-R), Kirchhoff approximation (KA), ocean waves, polarization, scattering.**

I. Introduction

IT IS NOW WELL recognized that navigation signals reflected off the sea surface can be used to investigate properties of the ocean surface. This technique, known as Global Navigation Satellite System Reflectometry (GNSS-R), has been extensively studied in recent years to demonstrate that the reflected signals contain useful information about the sea surface roughness, linked to ocean surface wind and waves [1]–[9], as well as the sea surface height [10]–[12]. The scatterometric applications of GNSS-R are quite well established, with recent studies showing the possibility of retrieving the directional mean square slopes (DMSSs) from reflected GPS signals collected both from airborne [5] and Low-Earth-Orbiting satellite [6] platforms. In both cases, the DMSSs were extracted from the delay–Doppler map (DDM), a 2-D representation of the scattered signal power in the delay and Doppler domains. The inversion methodology relied on the least square fitting of the observed DDM with a simulated DDM based on the well-known theoretical model by Zavorotny and Voronovich [1] (hereafter referred to as the Z-V model). The Z-V model provides an analytical expression of the average scattered power for GNSS signals in a bistatic forward scattering configuration under the Geometrical Optics (GO) scattering limit. The average scattered power depends on the roughness of the ocean surface through the 2-D probability density function (PDF) of the slopes of the large-scale surface roughness. In the case of linear ocean waves, the PDF is Gaussian and entirely characterized by the DMSS in two orthogonal directions. Clarizia *et al.* [6] applied the Z-V model to fit DDMs from the UK-DMC satellite. The study showed good general agreement between the spaceborne DDMs and the theoretical model, and the retrieved DMSS compared favorably against *in situ* measurements from buoys. Yet, the study also highlighted substantial differences in the structure and power distribution of the measured DDM compared with those simulated with the Z-V model, particularly away from the specular reflection point, where patchy patterns seen in the data were missing in the simulated DDMs. These differences may be due to several factors. Residual speckle noise due to the limited incoherent averaging time in the satellite observations could be partly responsible for the patchiness seen in the measured DDMs, which would not be present in the simulated Z-V DDMs for which the temporal averaging is effectively infinite. Other elements affecting the measured DDMs could be thermal noise in the receiver or limitations or problems in the receiver hardware. Conversely, it is also conceivable that the differences may originate from limitations of the modeling or from the simplified way of describing complex sea surfaces through a Gaussian PDF of the sea surface heights and slopes. In this paper, we chose to investigate the observed discrepancies through the use of

Manuscript received August 27, 2010; revised April 30, 2011; accepted June 12, 2011. Date of publication September 15, 2011; date of current version February 24, 2012.

M. P. Clarizia is with the School of Ocean and Earth Science, National Oceanography Centre, SO14 3ZH Southampton, U.K., and also with the Department of Engineering, University of Sannio, 82100 Benevento, Italy (e-mail: marari@noc.ac.uk).

C. Gommenginger and M. A. Srokosz are with the Marine Physics and Ocean Climate Group, National Oceanography Centre, SO14 3ZH Southampton, U.K.

M. Di Bisceglie and C. Galdi are with the Department of Engineering, University of Sannio, 82100 Benevento, Italy.

Digital Object Identifier 10.1109/TGRS.2011.2162245

0196-2892/$26.00 © 2011 IEEE

explicit 3-D representations of the sea surface and by adopting the more general theoretical framework of the Physical Optics (PO) scattering approximation [also known as the Kirchhoff approximation (KA)] in order to simulate the forward scattering of L-band signals from the sea surface. The aim is not to propose a new model to fit spaceborne GNSS-R data from large glistening zones (GZs) but rather to develop a flexible tool to investigate the interactions and mechanisms on the sea surface that affect the GNSS signal scattering and determine how to produce simulated DDMs that are closer to the observations. Explicit representations of the sea surface allow us to consider a much wider range of sea surface conditions, including complex combinations of wind waves and swell traveling in different directions. In this paper, we consider only ocean waves with linear Gaussian statistics, but the approach will allow future investigations of the impact of nonlinear ocean wave phenomena on GNSS-R ocean reflections. Hence, this approach offers new investigative capabilities, where we may consider how and to what extent different wind and wave conditions affect the GNSS scattering, and what further information may be extracted about nonlinear waves, whose influence on the skewness of PDFs has already been suggested based on real GNSS-R reflections [7]. In this paper, we simulate the scattering through a novel facet-based implementation of the KA applied to explicit sea surfaces. We will call this method the Facet Approach (FA). We will show that the FA retains the advantages of the full KA for the representation of the scattering properties (compared with the high-frequency GO approximation used in Z-V) but considerably simplifies the calculation of the KA by applying it to facets approximating the sea surface. As a result, the scattered field can be calculated directly for the large-scale roughness components present in a sea surface realization, thus depending on the actual features of the simulated sea surface rather than on a simple statistical description of the wave field. Simulating the scattering from individual sea surface snapshots also provides the flexibility of examining both the instantaneous scattered power from a given snapshot and the average scattered power obtained for an ensemble of successive snapshots. Another important difference of our approach is the use of a vector formulation to model the scattered field, as opposed to scalar formulation used in the Z-V model. This allows us to investigate polarization effects, the importance of which was previously recognized in [13] and the representation of which in large-scale scattering models was attempted recently by Thompson *et al.* [8] using a refined GO model based on a vector formulation. In the future, this facet-based approach will offer the possibility of combining the scattering from specific large-scale roughness features with the contribution from small-scale roughness components, by removing the assumption of flat facets and assuming the existence of ripples within a facet. This would give a two-scale representation of the GNSS-R scattering similar to the classical Two-Scale Model (TSM) [14], which would help to determine the relative contributions of different ocean scales to GNSS-R signals. Hereafter, we present details of the implementation of the facet-based bistatic scattering simulator. These include the simulation of 3-D explicit sea surfaces, the approximation of the sea surface by suitably sized facets given the KA roughness criteria, the calculation of the polarimetric instantaneous scattering of L-band monochromatic signals in a GNSS-R bistatic scattering configuration, and the comparison of the FA with the full KA and the Z-V model. The results in this study are presented primarily in the form of bistatic radar cross sections (RCSs), but an example of a DDM computed using the FA is also shown and compared with the DDM generated using the Z-V model. The influence of sea state and geometry on the DDMs is left to be examined in greater detail in a later publication. The analysis of the polarimetric RCS reveals interesting dependence between the scattered power and the structure of the wave field, particularly with regards to the polarization ratio (PR). Such polarimetric effects represent a significant result confirming the findings of Thompson *et al.* [8] that polarization effects consistent with observations can be obtained from improved modeling of the large-scale scattering, without the need to introduce small-scale (diffuse) scattering as it is done in many EM models. This paper is organized as follows. Section II introduces the large-scale microwave scattering problem, including consideration of the range of validity of the KA and the GO, and presents our FA. Section III reviews the criteria to be applied to determine the correct size of the facet in order to best approximate the sea surface while obeying the KA conditions of validity. Simulations and results are shown in Section IV, which is divided into the following sections: 1) simulations of sea surfaces with realistic waves in three cases of wind speeds with/without added swell (Section IV-A); 2) description of the configuration and scattering geometry and the characteristics of the transmitted signal (Section IV-B); 3) validation of the new FA against the KA and GO (Section IV-C); 4) results for the RCS for the three wind and wave simulations presented in Section IV-A; 5) polarization results for the three wind and wave simulations presented in Section IV-A; and 6) delay–Doppler mapping of the scattered power obtained with the FA and the Z-V model for a large GZ in a GNSS-R spaceborne scenario and for a single sea state (Section IV-F). Finally, Section V presents the conclusion from this study and outlines improvements and developments of the simulator to be completed in the future.

II. Simulating the Electromagnetic Scattering

In this section, we briefly review the main aspects of the KA and its high frequency limit, which is GO. Subsequently, we introduce the FA, which will be used for the evaluation of the scattering from the large-scale surface roughness.

A. The Kirchhoff Approximation

The KA [14]–[17], also known as Tangent Plane Approximation or PO, represents the scattering in a quasi-specular regime, and it is generally applicable when the local radius of curvature of the surface is much larger than the incident wavelength, namely [16]

$$\sqrt[3]{k_0 r_c}\cos(\theta) \gg 1 \tag{1}$$

where k_0 is the wave number of the incident radiation, r_c is the radius of curvature of the surface, and θ is the incidence

angle. The KA is an approximation of the exact solution of the Stratton–Chu equations [18] for the electric ($\mathbf{E^s}$) and magnetic ($\mathbf{H^s}$) fields scattered from a surface S. One formulation of the Stratton–Chu equation for the electric field is the following [17]:

$$\mathbf{E}^s = \frac{-jk_0}{4\pi R_2} e^{-jk_0 R_2} \iint_S \mathbf{p} e^{j\,\mathbf{q}\cdot\mathbf{r}}\, dS \tag{2}$$

with the vector $\mathbf{p}$ given by

$$\mathbf{p} = \hat{n}_s \times [\hat{n} \times \mathbf{E}^s - \eta_s\, \hat{n}_s \times (\hat{n} \times \mathbf{H}^s)] \tag{3}$$

and the other quantities defined as follows.

1) $\mathbf{q} = \mathbf{q}(\mathbf{r}) = k_0[\hat{n}_s(\mathbf{r}) - \hat{n}_i(\mathbf{r})]$ is the scattering vector, where $\hat{n}_s$ is the incident unit vector pointing from the transmitter to the scattering point $\mathbf{r}$ and $\hat{n}_s$ is the scattered unit vector pointing from the scattering point to the receiver.
2) $\hat{n} = \hat{n}(\mathbf{r})$ is the local normal to the surface at the reflection point.
3) η_s is the intrinsic impedance of the medium in which the electric field is scattered.
4) $\mathbf{E^s} = \mathbf{E^s}(\mathbf{r})$ and $\mathbf{H^s} = \mathbf{H^s}(\mathbf{r})$ are the scattered electric and magnetic fields on the interface S.
5) R_2 is the distance from the reflection point on the surface to the receiver.

The geometry of the surface-scattering problem is shown in Fig. 1. We now assume that the incident wave on the surface S is a spherical wave expressed as

$$\mathbf{E}^i = \frac{e^{-jk_0 R_1}}{4\pi R_1} \hat{a}\, E_0\, e^{-jk_0\, \hat{n}_i \cdot \mathbf{r}} \tag{4}$$

where $\mathbf{E_0}$ is the amplitude of the incident signal, R_1 is the transmitter range, and $\hat{a}$ is the incident unit polarization vector. The KA allows us to write the local fields $\mathbf{E^s}$ and $\mathbf{H^s}$ at a point on the surface S as the fields that would be produced by an infinite tangent plane at that point. This is applied separately for each polarization and translates into

$$\begin{aligned} \mathbf{E}^s_\perp &= R_\perp\, \mathbf{E}^i_\perp \\ \mathbf{H}^s_\parallel &= R_\parallel\, \mathbf{H}^i_\parallel \end{aligned} \tag{5}$$

where $\mathbf{H}^i_\parallel = \hat{n}_i \times \mathbf{E}^i_\parallel$. The terms $R_\perp$ and $R_\parallel$ are the Fresnel reflection coefficients for the two polarizations [17], and the subscripts $\perp$ and $\parallel$ denote the horizontally and vertically polarized components of the field, respectively, with respect to the local plane of incidence $(\hat{n}_i, \hat{n})$. The remaining polarized fields can be found as

$$\begin{aligned} \mathbf{E}^s_\parallel &= \eta_s \hat{n}_r \times \mathbf{H}^s_\parallel \\ \mathbf{H}^s_\perp &= \frac{1}{\eta_s} \hat{n}_r \times \mathbf{E}^s_\perp \end{aligned} \tag{6}$$

where $\hat{n}_r$ is the unit vector in the reflected direction (see Fig. 1). The fields $\mathbf{E}^s$ and $\mathbf{H}^s$ on the surface S can therefore be replaced by the sum of their vertically and horizontally polarized components, whose expressions are given in (5) and (6) and substituted into the vector term in (3) to obtain the scattered field $\mathbf{E}^s$ in (2). Finally, the bistatic normalized radar cross section (NRCS) can be defined as

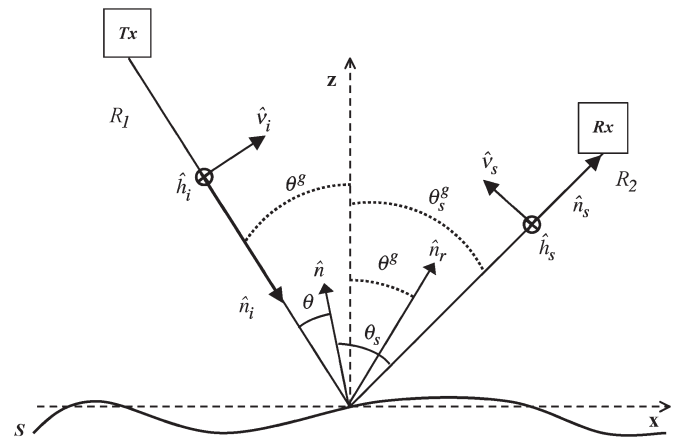

Fig. 1. Geometry of the surface scattering problem. The circled crosses indicate that the horizontal polarization vectors $\hat{h}_i$ and $\hat{h}_s$ are perpendicular to the plane of incidence x–z and directed into the page. Note that the global angles θ^g and θ^g_s are the incident and scattering angles relative to the global normal to the mean sea level (z-axis), whereas θ and θ_s are the local angles relative to the local normal $\hat{n}$ on S.

$$\sigma^0_{pq} = \frac{4\pi R_2^2\, \left|\mathbf{E}^s_{pq}\right|^2}{A\, \left|\mathbf{E}^i_{pq}\right|^2} \tag{7}$$

where A is the surface area and the subscripts p and q refer to the polarization of the incident and scattered field. Note that (7) gives us the means to compute both the copolarized (when $p = q$) and the cross-polarized (when $p \neq q$) NRCSs.

B. The Geometrical Optics Approximation

The KA provides an explicit form for the vector (3), but it still leaves the integral as a complicated function of the surface S and its local normal vectors and reflection coefficients. The most common and easy approximation is known as the GO or Stationary-Phase Approximation [1], [17]. This approximation considers that the scattering occurs only in the direction of specular reflection and removes the dependence of the vector $\boldsymbol{p}$ in the integral (2), leaving the exponential term as the only term in the integral. The total scattered field is the result of the superposition of the fields generated by a large number of specular points (mirrors) on the surface, reflecting the power in the direction of the receiver. The scattered power is evaluated as an ensemble average and, using some additional assumptions including Gaussian statistics for the sea surface elevations and slopes, can be evaluated in a closed form. This finally leads to the GO expression of the bistatic NRCS, given by [17]

$$\sigma^0_{pq} = \frac{\pi\, (k_0 q |U_{pq}|)^2}{q_z^4} P\left(-\frac{q_x}{q_z}, -\frac{q_y}{q_z}\right) \tag{8}$$

where U_{pq} are polarimetric coefficients (see [17, eq. (12.23)–(12.26)] for details); q_x, q_y, and q_z are x-, y-, and z-components of the scattering vector $\boldsymbol{q}$ and q is its norm; and $P(\cdot,\cdot)$ is 2-D Gaussian PDF of the slopes along the x and y coordinates.

The GO approximation is widely used, for its simplicity and ease of implementation, but it suffers some limitations. We will show in Section IV-C that, in the case where the transmitter and receiver lie in the x–z plane, as shown in Fig. 1, the GO shows no sensitivity to polarization other than through the Fresnel reflection coefficients. Furthermore, the average formulation of GO is a useful tool to quickly model the impact of surface roughness on the scattered field, but its parameterization of surface roughness with a Gaussian PDF effectively reduces complex surface roughness conditions to just two values of the variances of the surface slope to describe the sea surface. The average formulation thus prevents insight to be gained into the instantaneous behavior of the scattering and on how distinct features on the sea surface may affect the scattering.

C. The Facet Approach

Here, we illustrate our facet-based approach to calculate the scattering from large-scale surface roughness components based on solving the Kirchhoff integral (2) without the need for strong assumptions as in the case of GO. Equation (2) can indeed be simplified if we approximate the surface S by an ensemble of n planar facets, each of them tilted and oriented by the underlying long waves, and we solve the integral for each facet. We assume that all facets have equal projections of their sides along the x and y directions, namely, L_x and L_y, respectively. Each facet has a uniquely defined local normal. If the facet is sufficiently larger than the wavelength of the incident radiation, the EM fields are constant across the facet. The integral in (2) can be written as the sum of integrals over each facet as follows:

$$E^s = \sum_{k=1}^{n} E^{s,k} = -\frac{jk_0}{4\pi R_2} e^{-jk_0 R_2} \sum_{k=1}^{n} \iint_{S_k} \mathbf{p}^k \, e^{j\mathbf{q}\cdot\mathbf{r}} dS \quad (9)$$

where $\mathbf{p}^k$ is the vector $\mathbf{p}$ for the kth facet. The advantage of this approach lies in the fact that the integral for a single facet can easily be solved in a closed form. Indeed, with the vector $\mathbf{p}^k$ being constant over the facet, it can be taken out of the integral and can be evaluated by applying the KA through (3)–(6). At this point, the rest of the integral simply becomes the integral of an exponential term over a facet, whose tilt along x and y can be known. The final expression for the scattered field from the kth facet is

$$\begin{aligned}\mathbf{E}^{s,k} = &- jk_0 \, \mathbf{p}^k \frac{e^{-jk_0 R_2}}{4\pi R_2} \sqrt{1+\alpha_k^2+\beta_k^2} \, e^{-j\mathbf{q}\cdot\mathbf{r}^k} \\ &\cdot L_x L_y \operatorname{sinc}\left[(q_x + q_z\alpha_k)L_x/2\right] \\ &\cdot \operatorname{sinc}\left[(q_y + q_z\beta_k)L_y/2\right] \end{aligned} \quad (10)$$

where $\mathbf{r^k}$ is the coordinate of the central point of the kth facet, L_x and L_y are the side projections of the facet along x and y, respectively, and α_k and β_k are the derivatives of the surface along x and y at the central point of the kth facet. Here, the function $\operatorname{sinc}(x)$ is defined as $\sin(x)/x$. The total scattered field in (9) can be then evaluated by coherently summing the scattered fields from each facet given in (10). The sinc terms

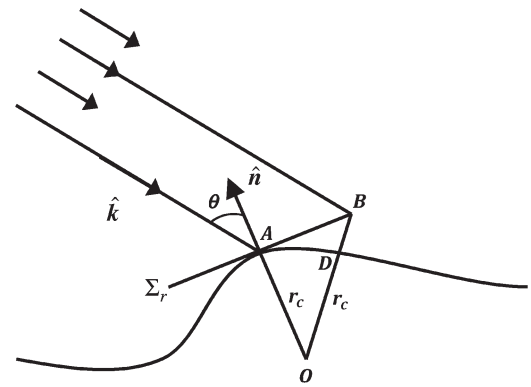

Fig. 2. Illustration of the tangent plane Σ_r and its local coordinate system, with the half-length AB of the facet and the distance from the underlying surface BD.

that appear in (10) clearly indicate that the FA treats the facets as radiating antennas, with a specific nonzero width main lobe, which allows some scattered power in directions away from the specular direction. The width of the sinc lobe decreases with increasing facet size, so that large facets have scattered power concentrated around the specular direction in a narrow lobe. Thus, the method seems to offer a more complete description of the scattering than GO, as it solves the KA for ensembles of finite-size facets approximating the sea surface. Furthermore, the FA displays more sensitivity to polarization with respect to formulations like the Z-V model commonly used to describe GNSS-R scattering. However, it is clear that the size of the facets is a key parameter that will determine the applicability of this new method. The choice of facet size will be a tradeoff between the need to comply with the KA conditions on roughness, the ability of the facets to adequately approximate the underlying sea surface, and computational expense. We discuss in the next section how the choice of facet size is not entirely arbitrary but governed by some specific important criteria.

III. Choosing the Facet Size

The criteria we adopt here for choosing the size of the facet stem from considerations first presented in [16] to discuss the applicability of the KA. These relate to the geometrical conditions shown in Fig. 2, which constitute the starting point for the formulation of the standard roughness criterion given in (1).

With reference to Fig. 2, it is considered that the reflection of an electromagnetic wave at a point A on the surface can be taken to occur as if from a tangent plane centered at that point, if one can identify a region on the tangent plane Σ_r with linear dimensions which are large relative to the EM wavelength, but which also does not deviate noticeably at the edges of the region from the underlying surface. This region on the tangent plane is what we define as a facet. The aforementioned argument translates into the two mathematical conditions [16]

$$AB \gg \frac{1}{k_0 \cos(\theta)} \quad (11)$$

$$BD \ll \frac{\cos(\theta)}{k_0} \quad (12)$$

where AB and BD are the segments shown in Fig. 2. We can easily see that

$$BD = OB - OD = \sqrt{AB^2 + r_c^2} - r_c \tag{13}$$

where r_c is the local radius of curvature of the surface. Thus, we can express both (11) and (12) in terms of AB as

$$AB \gg \frac{1}{k_0 \cos(\theta)} \tag{14}$$

$$AB \ll \sqrt{\left[\frac{\cos(\theta)}{k_0}\right]^2 + 2\frac{r_c \cos(\theta)}{k_0}}. \tag{15}$$

In our case, AB represents half the facet size, and criteria (14) and (15) will be used to determine the appropriate facet size. It is worth noting that the inequalities (14) and (15) can be more or less difficult to satisfy, depending on the quantitative interpretation of the much greater than and much smaller than inequality signs. We could choose to interpret those as AB having to be larger (or smaller) than the term on the right-hand side by a factor of, for example, at least 10. While inequality (14) is easily satisfied with a factor of 10, inequality (15) with such a factor becomes a very stringent condition. This would either imply the use of very small facets or reduce the applicability of KA to only the calmest sea-state conditions. In our simulations, we will relax the condition for inequality (15) by considering a factor smaller than 10, which allows the use of larger facets ($\sim$1 m) to approximate the sea surface. It is interesting to note that if we combine (14) and (15) in a manner similar to what is done in [16], we obtain a condition similar to the standard applicability condition (1) of the KA, namely

$$\sqrt[3]{2k_0 r_c} \cos(\theta) \gg \sqrt[3]{1 - \cos^4(\theta)}. \tag{16}$$

For simplicity, in our simulations, we will use the standard KA condition (1) to define what constitutes large-scale surface roughness compliant with KA and the conditions (14) and (15) to determine the size of the facets.

IV. Numerical Simulations and Results

This section is organized in six sections where we investigate the most important features and limitations of the simulator implemented so far to represent the scattering of GNSS-R signals from ocean surfaces. First, we briefly present how we generate 3-D surfaces with realistic wave fields and show examples for three different wind speed and swell conditions. Next, we introduce some key concepts about the geometrical configuration of the scattering scenario and the characteristics of the signals, and we analyze the results of the FA, comparing it with both the GO and a numerical implementation of the full KA. Then, we examine the instantaneous and average NRCS and PR for the three different sea surface simulations to investigate how sea surface conditions affect the scattered signals. Finally, we present an example of the DDM of scattered power computed using FA for a specific sea state, and we compare it with a DDM obtained using the Z-V model for the same sea state.

A. Simulations of the 3-D Realistic Ocean Wave Fields

The generation of ocean surface maps was carried out using a well-established technique based on filtering a white Gaussian process with a specified theoretical wave spectrum. This approach preserves the Gaussian statistics of the sea surface elevations and slopes while allowing us to specify particular spectral properties of the wave field. It is worth recalling here that our objective is to simulate the large-scale roughness of the ocean only, since we are not considering the scattering from small-scale features at this stage (for which the diffusive EM scattering needs to be calculated using a different approximation). This means that a wave number cutoff needs to be chosen to identify the components that constitute the large-scale roughness. Only the spectral components of the spectrum for wave numbers below that wave number cutoff will contribute to the generation of the sea surface. Several attempts exist in the literature to propose an objective method to choose this cutoff [1], [2], [8] but there is no consensus. In our case, we determined the cutoff experimentally by simulating the sea surfaces for a given cutoff and by evaluating numerically the radii of curvature of the surface to verify *a posteriori* that they satisfy the KA criterion defined by (1).

The ocean wave spectrum used to filter the white Gaussian process was the theoretical directional wave spectrum model by Elfouhaily *et al.* [19]. This model produces a wave field entirely defined by the wind speed and the wind direction. Two examples of wind-generated surfaces are shown in Fig. 3(a) and (b) corresponding to wind speeds of 5 and 10 m/s, respectively. In all cases, the wind direction is 0° with respect to the x-axis.

The simulated surfaces are generated with a resolution of 20 cm and are 500 by 500 m, large enough to include a sufficient number of dominant ocean wavelengths for both wind speeds. In the case of the 10-m/s wind speed, the surface is able to capture on the order of five dominant wavelengths. The cutoff wavelength used to simulate these surfaces was equal to 1 m, equivalent to five times the incident radar wavelength in the case of L-band. This is not a very high wave number cutoff, and it does not impose excessive filtering of the original surface. We checked *a posteriori* that this cutoff produces a surface that satisfies the KA criterion, where (1) was computed using the global incidence angle θ^g (see Fig. 1) and the median radius of curvature of the surface in the direction of the wind (x-axis). Note that the median radius of curvature of the surface in the direction of the wind will be smaller than in other directions due to the geometry of the wave field (see Fig. 3).

In Fig. 3(c), we show the 10-m/s wind wave field from Fig. 3(b) with an added swell, modeled as a simple 2-D sinusoidal wave with amplitude of 1 m and wavelength of 100 m and traveling in a direction 60° from the wind direction (clockwise from the x-axis). This last example illustrates how these explicit sea surface simulations give the flexibility to consider realistic and more complex sea states, featuring coexisting wind and swell waves traveling in different directions, which cannot be represented using a simple PDF of slopes.

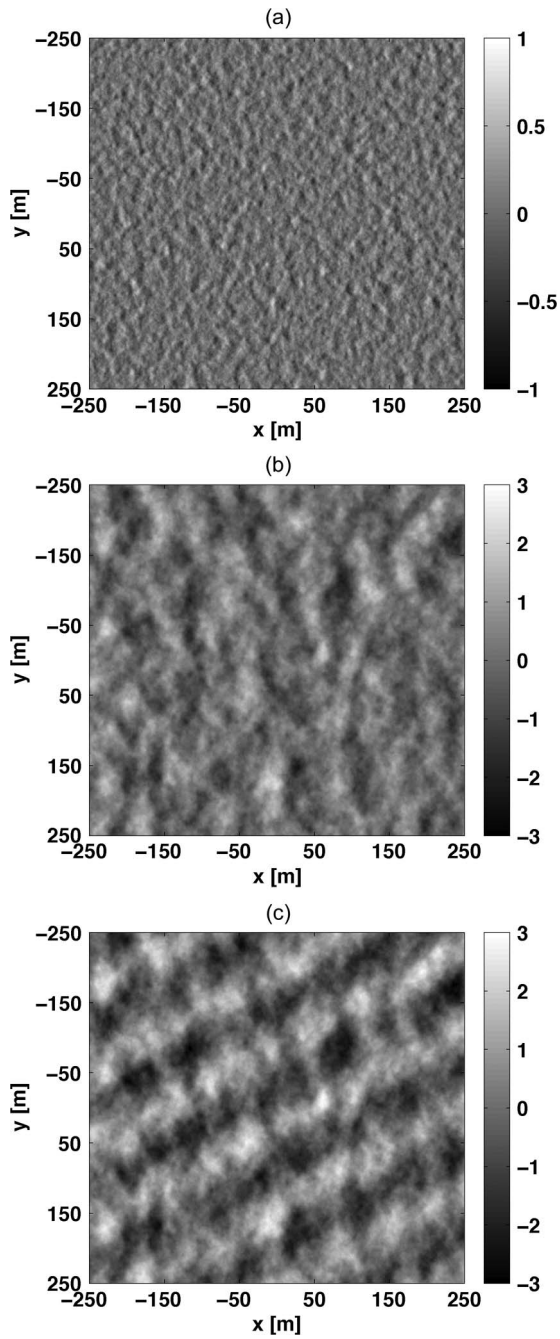

Fig. 3. Three-dimensional ocean wave field over 0.5 km × 0.5 km generated with a 20-cm resolution and a cutoff wavelength of 5 $\lambda_{\text{L-band}}$ (∼1 m). The three subplots correspond to the following: (a) Wind waves for wind speed of 5 m/s, (b) wind waves for wind speed of 10 m/s, and (c) wind waves for wind speed of 10 m/s plus added swell with amplitude of 1 m, wavelength of 100 m, and direction of 60° clockwise with respect to the x-axis. The wind direction is along the x-axis in all cases. Units in grayscale are meters.

B. Configuration of the Scattering Scenario

As shown in Fig. 1, the transmitter and the receiver lie in the $x-z$ plane. In our simulations, the transmitter and receiver are in a spaceborne configuration and their ranges are 20 000 and 680 km, respectively. These correspond to the typical altitude of transmitting satellites in navigation system constellations like GPS and the Low-Earth-Orbiting altitude of the UK-DMC satellite [4], [6]. The position of the transmitter is fixed with a constant range R_1 and incidence angle $\theta^g = 20°$. The receiver range R_2 is also fixed while its scattering angle is variable and indicated by θ_s^g in Fig. 1, which ranges from $-10°$ to $50°$ from the global vertical. The specular direction corresponds to a scattering angle θ_s^g equal to $20°$. The incident wave is an L-band $(= 19$ cm$)$ spherical wave, as expressed in (4), with unitary amplitude. At this stage, it is convenient to introduce the horizontal and vertical unit polarization vectors $\hat{h}_i$, $\hat{v}_i$ for the incident wave and $\hat{h}_s$, $\hat{v}_s$ for the scattered wave, defined with respect to the plane of incidence $(\hat{n}_i, \hat{z})$ and the scattering plane $(\hat{n}_s, \hat{z})$, respectively. Given that both the transmitter and the receiver lie in the x–z plane, the incident and scattered polarization vectors can be simply expressed as

$$\begin{aligned}
\hat{h}_i &= \hat{y} \\
\hat{v}_i &= -\hat{x}\cos(\theta^g) - \hat{z}\sin(\theta^g) \\
\hat{h}_s &= \hat{y} \\
\hat{v}_s &= \hat{x}\cos\left(\theta_s^g\right) - \hat{z}\sin\left(\theta_s^g\right).
\end{aligned} \tag{17}$$

Two cases of incident polarization have been considered: The first is horizontal polarization $(\hat{h}_i)$, and the second is vertical polarization $(\hat{v}_i)$. Although it is recognized that real GNSS signals are right hand circularly polarized, the scattering model is expressed here in terms of its linear polarization components, in the hope to gain more insight into physical processes at the ocean surface. The results for circular polarization are easily derived from these, since circular polarization is simply of a linear combination of the linear polarization components.

C. Validation of the FA

An initial set of simulations was generated to compare the results of the FA with the GO and a numerical implementation of the full KA. The latter was obtained by computing the KA integral given in (2) with a standard numerical integration method, applied to a new realization of the sea surface generated at much higher resolution than for the FA. Due to computational limits, this full KA method can only be applied for relatively small areas of the ocean surface. However, the surface must be large enough to include a sufficient number of dominant ocean wavelengths to ensure that the scattering is statistically representative of all relevant processes on the surface. The dimensions of the new surface realization were 50 m by 50 m, generated with a very high spatial resolution of 2 cm. This calculation was performed for a wind speed of 4 m/s aligned along the x-direction. This low wind speed ensures that the 50 × 50 m surface can represent about three dominant ocean wavelengths (about 17 m for a 4-m/s Elfouhaily spectrum). Similarly, we calculated the scattered RCS for the GO for the same wind speed conditions using (8).

For the implementation of the FA, we need to choose the size of the facet based on inequalities (14) and (15) introduced in Section III. As discussed previously, the size of the facet is a tradeoff between the need to properly represent the underlying sea surface (for which large number of small facets is best) and the need to obey the KA roughness conditions (for which fewer larger facets is more suitable). In our case, using the same angle and radius of curvature as in the Kirchhoff criterion, the conditions (14) and (15) require the facet size to be greater than

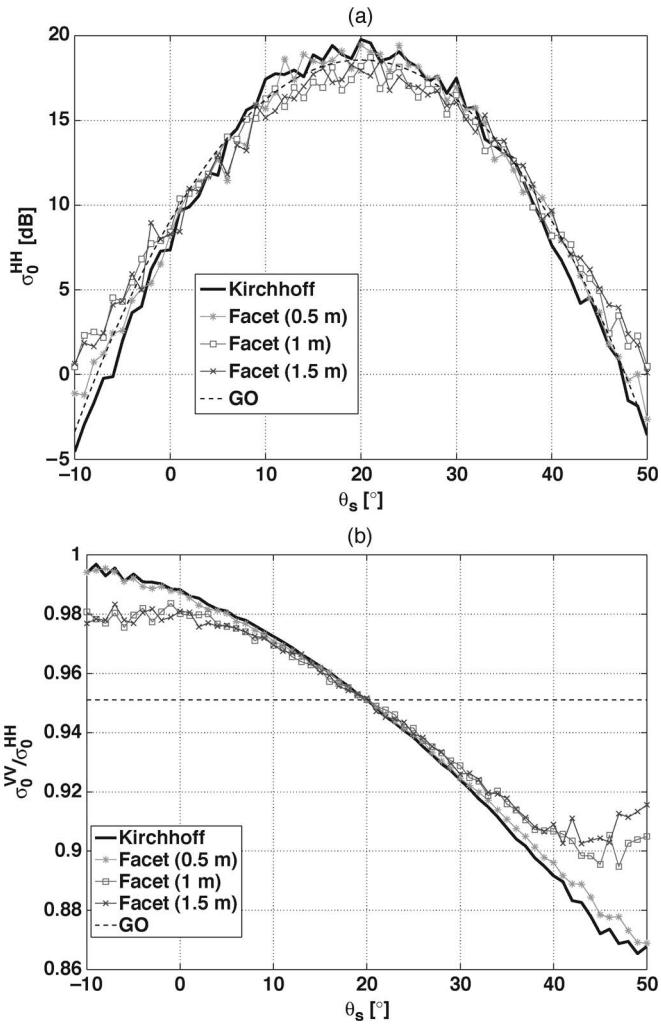

Fig. 4. (Top) Horizontal copolarized NRCS and (bottom) PR plotted against scattering angle for the full KA, the GO, and the FA with three choices of facet size. The results were averaged over 50 sea surface realizations for a wind speed of 4 m/s. The scattering angle value of 20° corresponds to the specular direction.

0.06 m and less than 1.6 m. We therefore present the FA results for three facet sizes (0.5, 1, and 1.5 m) to be compared against the GO and the full KA.

Fig. 4(a) shows the averaged horizontal copolarized (HH) NRCS in decibels calculated using (7) as a function of the scattering angle θ_s^g. The NRCS was averaged over 50 realizations of the sea surface for a wind speed of 4 m/s. The results are shown for an overall angular interval of 60° centered on the specular direction, which is at 20° from the vertical and corresponds to the direction of maximum forward scattering. The average NRCS is shown for HH polarization only, as results for VV polarization were similar.

From Fig. 4(a), we see that the NRCS calculated using the FA is in good agreement with the full KA for all three facet sizes and that they all exhibit oscillations that are comparable with the KA curve. The NRCS from the FA are slightly lower than the KA within 20° of the specular direction (for scattering angles between 0° and 40°) and become slightly higher than the KA further away from the specular direction. As expected, the FA computed with the smallest facet size (0.5 m) gives the closest results to the KA. The FA results corresponding to 1.5 m facets, close to the upper limit of the facet size condition, differs most from the KA, by approximately 2 dB around the specular point. The patterns and oscillations in the NRCS also seem to become more different from those of the KA curve when the facet size increases. The FA led to a large reduction in computation times compared with the full KA. For facet size of 0.5 m, the FA computations were faster by a factor of almost 600, while for facet size of 1.5 m, the improvement in computation time was by more than 7000. The reduced computation time represents an important benefit of the FA, where larger facets lead to lower computational cost and the ability to handle larger surfaces, while still providing a reasonable level of accuracy compared with the full KA. Fig. 4(a) also shows the NRCS evaluated with the GO through (8). The variance of the Gaussian slopes (MSS) was computed through integration of the Elfouhaily *et al.* slope spectrum [19] up to the same wave number cutoff as used for the simulation of the explicit surface. The GO results are close to the full KA. GO thus provides a good approximation of the scattering, in an easy to implement method. However, as discussed previously, GO offers only limited means of exploring polarization and the scattering from complex sea surfaces. In order to investigate polarization effects, we use the PR, defined as

$$PR = \frac{\sigma_{\mathrm{VV}}}{\sigma_{\mathrm{HH}}}. \tag{18}$$

Fig. 4(b) shows the PR for the full KA, the FA for three different facet sizes, and the GO, again as a function of the scattering angle. In all cases, the PR is lower than 1, evidence that the scattered HH component is always stronger than the scattered VV component. It is interesting to note that the PR computed with the FA shows sensitivity to polarization similar to the full KA, both showing a decrease of the PR with increasing scattering angles. This indicates that the scattered HH component becomes larger than the scattered VV component as one moves away from the specular direction. The PR exhibits the same behavior around the specular direction for the KA and FA for all the facet sizes. Some differences appear between the KA and FA away from the specular direction, with the smallest facet size showing best agreement with KA over the widest range of angles (as expected). We note also the deterioration in the ability of the FA to match the KA at angles more than 10° from the specular direction when the facet size increases from 0.5 to 1 m. As expected, the PR for the GO shows no variation with respect to the scattering angle and it is simply equal to the ratio of the vertical and horizontal polarization Fresnel reflection coefficients of seawater. Note that the PR for the GO matches the value of the PR for the full KA and the FA in the specular direction.

D. Scattering Results for Different Wind and Wave Conditions

We present the copolarized HH NRCS calculated with the FA for simulated wave fields obtained at two different wind speeds and in the presence of a swell (see Section IV-A). Cross-polarized components of the NRCS (HV and VH) were also computed and analyzed but are not shown, as they display much

lower levels than the copolarized components and no features of interest. The copolarized results are first presented in the form of instantaneous 2-D maps, where each point represents the value for one individual facet. The specular point is located at the center of the maps, and the receiver is located in the specular direction. Here, the facet size is chosen to be 1 m $\times$ 1 m, as the computations are now for 500 m $\times$ 500 m areas of the sea surface. Fig. 5 shows the instantaneous HH copolarized bistatic NRCS in decibels for the simulated wave fields shown in Fig. 3. It is worth mentioning here that these images do not represent the power scattered from the sea surface, as sensed by a receiver, since they do not account for the phase of the scattered field from each facet. The phase plays a major role when combining the contributions from all facets (as shown later). Nevertheless, these maps are useful to examine the spatial distribution of the scattered power and how the GZ (the area contributing to the forward scattering) looks for different sea conditions and different geometrical configurations. The NRCS in Fig. 5 appears relatively uniform across the surface. This is because we are in a spaceborne configuration and the simulated surface covers only the small central part of the GZ around the specular point, corresponding to a small range of scattering angles away from the specular direction. Interestingly, the NRCS exhibits some wave patterns that show a good degree of correlation with the corresponding wave field, particularly in the high-wind-speed and high-wind-speed-plus-swell cases [Fig. 3(b) and (c)]. The NRCS is larger in the low-wind case [Fig. 5(a)] and decreases for higher wind speed cases [Fig. 5(b) and (c)], which is consistent with our expectations of decreased scattering in the specular direction when the sea gets rougher. Diagonal wave patterns aligned with the swell wave crests can be seen in Fig. 5(c), indicating a detectable influence of this particular swell train on the distribution of the scattered power in the GZ.

Next, we examine the average NRCS for the whole surface, computed by coherently summing the complex scattered fields from all facets and taking into account the phase of the scattered field from each facet. The average NRCS is shown in Fig. 6 for various positions of the receiver over a range of scattering angles up to 30° on either side of the specular direction. Fig. 6 shows the average HH NRCS for simulations at two different wind speeds. The NRCS results were averaged over 50 realizations of the sea surface in order to reduce the variability due to the individual waves in single realizations. The sensitivity of the average NRCS to wind speed is clearly visible. We note again the lower NRCS for higher wind speed in the specular direction and the slower decay away from the specular direction when the surface is rougher. Again, this is consistent with our expectation of increased scattering away from the specular direction at higher wind speeds. The same computation was done also for the wind-sea-plus-swell case [Fig. 3(c)], but the results are not shown as we could not identify any significant difference from the wind-sea-only case for the same wind speed.

E. Scattering Results for Different Polarizations

Here, we investigate the polarimetric signature of the forward scattering by examining the spatial distribution of the PR, calculated from the instantaneous NRCS presented in the previous section. Fig. 7 shows the PR for the simulated wave fields shown in Fig. 3. The spatial maps immediately reveal that the PR is clearly correlated with the underlying wave field, the PR exhibiting crests-and-troughs patterns closely matching those of the waves. In Fig. 7(c), the presence and directionality of the swell is easily detected as an oblique pattern across the surface aligned with the line of the swell wave fronts. We see

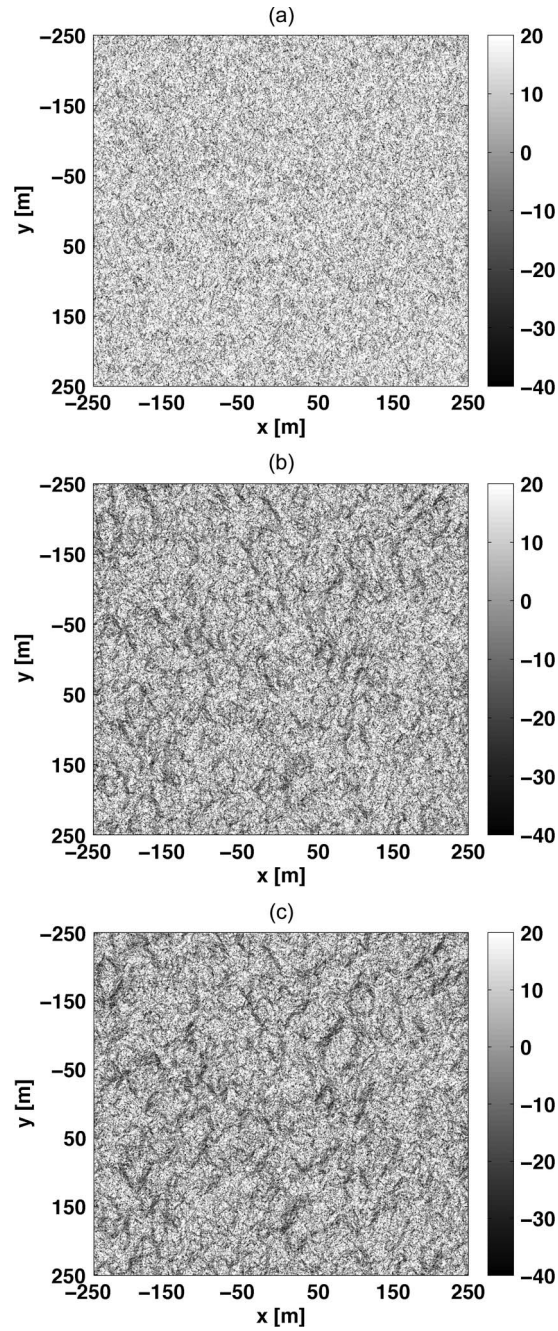

Fig. 5. Spatial maps of instantaneous copolarized HH bistatic NRCS in decibels computed with the FA and a facet size of 1 m^2. Each pixel represents the scattering from a single facet. The three subplots correspond to the simulated wave fields shown in Fig. 3, i.e., (a) wind waves for wind speed of 5 m/s, (b) wind waves for wind speed of 10 m/s, and (c) wind waves for wind speed of 10 m/s plus added swell with amplitude of 1 m, wavelength of 100 m, and direction of 60° clockwise with respect to the x-axis. The wind direction is along the x-axis in all cases.

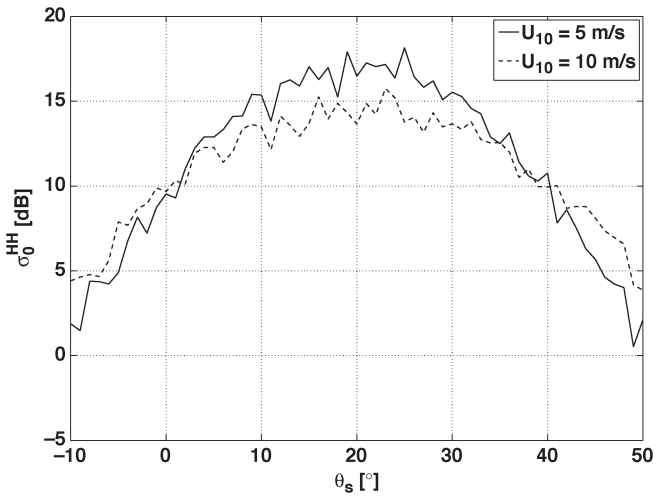

Fig. 6. Average HH NRCS in decibels computed with the FA and a facet size of 1 m^2 plotted against scattering angle. The specular direction corresponds to the scattering angle value of 20°. Results are shown for simulations at (solid line) 5 m/s and (dashed line) 10 m/s. The results were averaged over 50 realizations of the sea surface.

that the PR is generally less than 1, with marked minima in the troughs of the waves, indicating a stronger HH component for the scattering originating in the troughs of the waves. As for the NRCS, we computed the average PR for a range of scattering angles and different wind speed and wave conditions. We found that the average PR for the different simulated sea states (not shown) exhibits no marked differences, except a long way from the specular direction, where the validity of the FA starts to break down.

F. Delay–Doppler Mapping of the Scattered Power

In this section, we show an example of a noise-free single-look DDM of the scattered power computed using the FA, from a single sea surface snapshot. The sea surface is now a large area of 100 km by 100 km, which is comparable to the size of a typical GZ in a spaceborne GNSS-R configuration. The sea surface has been generated using a resolution of 0.2 m, a cutoff wavelength of 1 m, and a wind speed of 10 m/s. The scattering has been calculated using facets of 1 m by 1 m, and the complex scattered fields from each facet have been coherently accumulated in DD domain, thus taking into account the phase with which each facet scatters. Following the mathematical steps for the GPS-R receiver implementation outlined in [6], the Woodward Ambiguity Function of pseudorandom GPS sequences has been applied to each DD pixel of scattered field to simulate the effect of the GPS-R receiver matched filter. Finally, the resulting complex DDM of scattered field has been converted into a DDM of scattered power by simply taking the squared absolute value. Fig. 8(a) shows the DDM computed from FA in normalized units. For comparison, a DDM of the scattered power computed from the Z-V model is shown in Fig. 8(b). For Z-V, the two components of the MSS have been computed through integration of an Elfouhaily *et al.* [19] surface wave spectrum for a 10-m/s wind speed, up to the cutoff wavelength of 1 m specified in Section IV-A. Here, we must emphasize that although both FA and Z-V correspond to the same sea-state

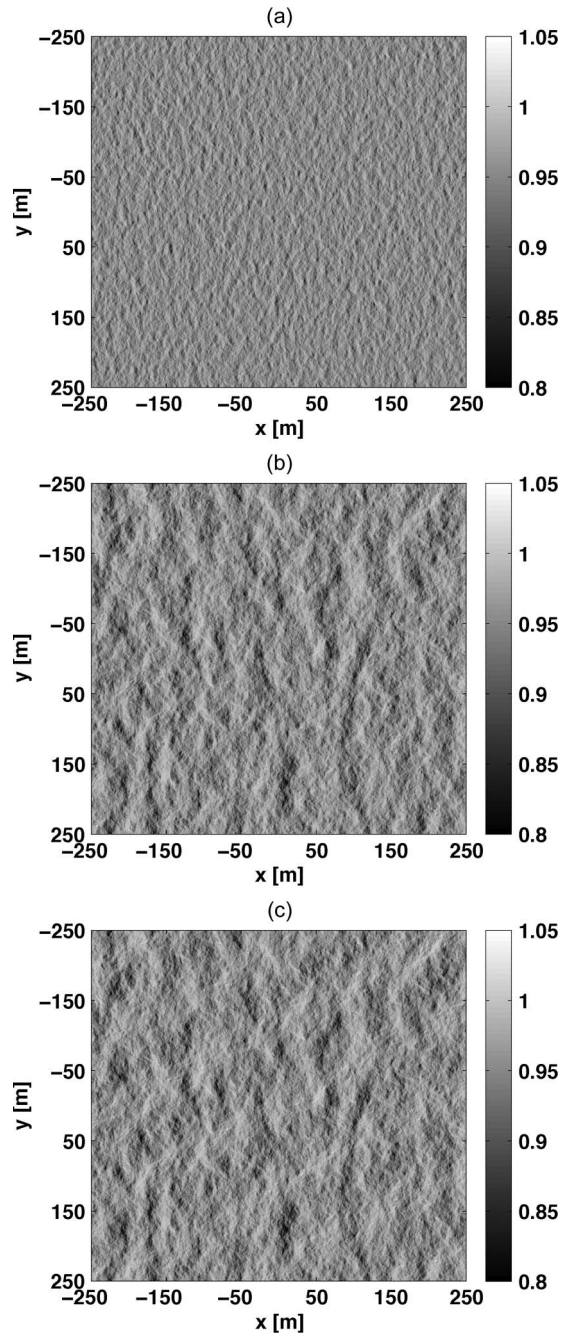

Fig. 7. PR based on the instantaneous VV and HH NRCSs computed with the FA and a facet size of 1 m^2. Each pixel represents the PR for a single facet. The three subplots correspond to the simulated wave fields shown in Fig. 4(a), i.e., (a) wind waves for wind speed of 5 m/s, (b) wind waves for wind speed of 10 m/s, and (c) wind waves for wind speed of 10 m/s plus added swell with amplitude of 1 m, wavelength of 100 m, and direction of 60° clockwise with respect to the x-axis. The wind direction is along the x-axis in all cases.

conditions, the FA and the Z-V DDM are not exact equivalents, since the Z-V DDM corresponds to a statistical average of the scattered power over an infinite number of looks whereas the FA-DDM represents the distribution of power from a single deterministic sea surface realization. Accordingly, while the FA DDM exhibits the same overall horseshoe shape as Z-V, it also presents a more patchy structure than Z-V. We find (not shown) that the patches occur in different positions in the DD domain for different sea surface realizations, indicating

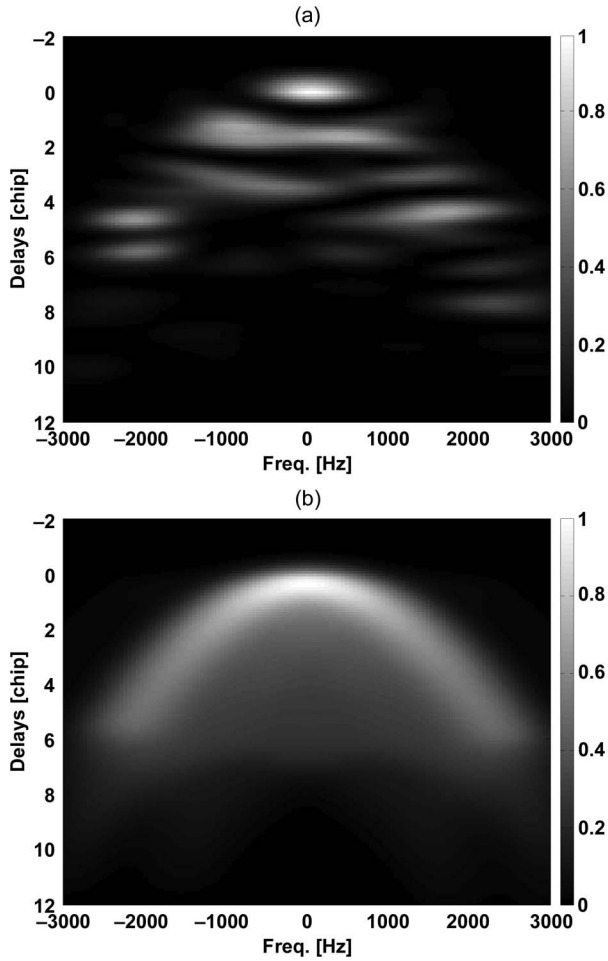

Fig. 8. DDMs for a 100-km^2 GZ and a 10-m/s wind speed, computed using a 50-Hz Doppler resolution and 0.1 chip delay resolution (1 chip $\sim$ 1 μs). (a) DDM computed using FA and 1-m^2 facets. (b) DDM computed using the Z-V model.

that it clearly corresponds to an instantaneous representation in DD space of the scattered power from particular features in each sea surface realization. We also find that, for FA, a considerable amount of scattered power is present both between the branches of the horseshoe and for large delay and Doppler values along the horseshoe, where the Z-V model predicts very weak scattering. The DDMs simulated using the FA therefore exhibits some interesting patterns that show similarities to the measured DDMs on UK-DMC [6]. The response of single-look DDM to different and more complex underlying sea surface conditions will be investigated in more detail in a future paper, together with comparisons with the Z-V DDM after incoherent accumulation of multiple single-look DDMs computed with the FA.

V. Conclusion

We have presented a new facet-based approach to model the forward scattering of monochromatic signals at L-band from realistic rough sea surfaces and have illustrated its application to compute DDMs for a spaceborne GNSS-R configuration. Rough ocean surfaces were generated for the cases of wind waves only and of more complex composite wave fields containing both wind waves and swell traveling in different directions. The electromagnetic scattering was computed through a novel facet-based implementation of the KA, which we call the FA. The method approximates the rough sea surfaces with a large number of small facets, representative of the large-scale roughness of the wave field. The scattered power is calculated for each facet in a closed form, and the facet size is chosen according to specific criteria. The FA scattering results were validated against the full Kirchhoff integral and the GO, which is the model most commonly used in GNSS-R. The FA proves a versatile tool to investigate the relation between the forward scattering and the ocean wave field. With respect to GO, the FA shows more sensitivity to polarization and provides the flexibility to investigate both instantaneous maps of the scattered power fields and average scattered power for different scattering angles. The FA was shown to provide comparable accuracy with that of the full Kirchhoff integral, with the advantage of much lower computational expense, and consequently provides the ability to compute the forward scattering from larger surfaces.

Instantaneous spatial maps of the bistatic NRCS and the PR for three different wind and wave conditions show clear correspondence between the distribution of the scattering and the underlying wave field. The presence of swell traveling in a different direction from the wind is detectable in the spatial distribution of instantaneous NRCS, but its effect is not evident in the average NRCS calculated for the whole surface. The behavior of the average NRCS with respect to wind speed is consistent with increased scattering away from the specular direction as surfaces become rougher as the wind speed increases. As regards polarization, the HH component of the scattered field is consistently larger than the VV component, particularly in the troughs of the ocean waves. Spatial maps of the PR exhibit crest-and-trough patterns strikingly similar to the underlying wave field. Once again, the swell component used in this study and its direction are easily detectable from the spatial maps of the PR. However, the average PR for the whole surface shows little sensitivity to sea state, except in scattering directions far away from the specular direction, where the validity of the FA and the KA is questionable.

An example was presented of a DDM of the scattered power calculated using FA for a large GZ corresponding to a spaceborne GNSS-R scenario. A preliminary comparison with a DDM obtained using the Z-V model for the same sea surface conditions reveals clear differences in overall structure, with the FA-DDM exhibiting interesting patchy features and a broader distribution of the scattered power across the DD domain than seen in Z-V, similarly to the measured DDM from UK-DMC [6].

The proposed facet-based approach has provided interesting insight on the influence of waves on the spatial distribution of the instantaneous scattered power and the PR and some encouraging results when mapping the scattered power in the Delay Doppler domain. The natural next step is to exploit this tool to investigate what characteristics of the wave field have a detectable signature in DDMs. The simulator should help to determine what properties of the ocean surface can be derived from measured DDMs from spaceborne GNSS-R receivers such as UK-DMC. Due to the ability of the FA to

compute the forward scattering for complex surface conditions, defined explicitly through 3-D ocean surfaces, this approach also offers the possibility of analyzing the scattering for more complex combination of linear ocean waves, as well as for ocean surfaces featuring steep nonlinear ocean waves with non-Gaussian statistics.

Finally, this work also revealed some relevant polarization effects in L-band bistatic scattering over the ocean. The polarimetric signature obtained with the FA confirms earlier findings [8] that polarization effects can be reproduced by considering a more comprehensive description of the large-scale scattering, such as provided by the KA. In the future, the facet-based approach could also be enhanced to include a diffuse scattering contribution due to small-scale roughness by considering slightly rough facets. This would lead to a TSM where the large-scale scattering is governed by the deterministic features on the surface and the small-scale scattering is described statistically. The simulator could then be used to ascertain the relative importance of large- and small-scale roughness contributions to GNSS-R signals.

Acknowledgment

The authors would like to thank V. Zavorotny from the Earth Systems Research Laboratory, National Oceanic and Atmospheric Administration, and D. Thompson from the Applied Physics Laboratory, Johns Hopkins University, for their useful feedback and discussions, and the anonymous reviewers for their thorough reviews, helpful comments, and observations.

References

[1] V. Zavorotny and A. Voronovich, "Scattering of GPS signals from the ocean with wind remote sensing applications," *IEEE Trans. Geosci. Remote Sens.*, vol. 38, no. 2, pp. 951–964, Mar. 2000.

[2] J. Garrison, A. Komjathy, V. Zavorotny, and S. J. Katzberg, "Wind speed measurements using forward scattered GPS signals," *IEEE Trans. Geosci. Remote Sens.*, vol. 40, no. 1, pp. 50–65, Jan. 2002.

[3] A. Komjathy, M. Armatys, D. Masters, P. Axelrad, V. Zavorotny, and S. Katzberg, "Retrieval of ocean surface wind speed and wind direction using reflected GPS signals," *J. Atmos. Ocean. Technol.*, vol. 21, no. 3, pp. 515–526, Mar. 2004.

[4] S. Gleason, S. Hodgart, S. Yiping, C. Gommenginger, S. Mackin, M. Adjrad, and M. Unwin, "Detection and processing of bistatically reflected GPS signals from Low-Earth Orbit, for the purpose of ocean remote sensing," *IEEE Trans. Geosci. Remote Sens.*, vol. 43, no. 6, pp. 1229–1241, Jun. 2005.

[5] O. Germain, G. Ruffini, F. Soulat, M. Caparrini, B. Chapron, and P. Silvestrin, "The Eddy experiment: GNSS-R speculometry for directional sea-roughness retrieval from low altitude aircraft," *Geophys. Res. Lett.*, vol. 31, p. L12 306, Nov. 2004.

[6] M. Clarizia, C. Gommenginger, S. Gleason, M. Srokosz, C. Galdi, and M. D. Bisceglie, "Analysis of GNSS-R delay–Doppler maps from the UK-DMC satellite over the ocean," *Geophys. Res. Lett.*, vol. 36, p. L02 608, Jan. 2009.

[7] E. Cardellach and A. Rius, "A new technique to sense non-Gaussian features of the sea surface from L-band bistatic GNSS reflections," *Remote Sens. Environ.*, vol. 112, no. 6, pp. 2927–2937, Jun. 2008.

[8] D. Thompson, T. Elfouhaily, and J. Garrison, "An improved Geometrical Optics model for bistatic GPS scattering from the ocean surface," *IEEE Trans. Geosci. Remote Sens.*, vol. 43, no. 12, pp. 2810–2821, Dec. 2005.

[9] J. Marchan-Hernandez, N. Rodriguez-Alvarez, A. Camps, X. Bosch-Lluis, I. Ramos-Perez, and E. Valencia, "Correction of the sea state impact in the L-band brightness temperature by means of delay–Doppler maps of global navigation satellite signals reflected over the sea surface," *IEEE Trans. Geosci. Remote Sens.*, vol. 46, no. 10, pp. 2914–2923, Oct. 2008.

[10] M. Martin-Neira, M. Caparrini, J. Font-Rossello, S. Lannelongue, and C. S. Vallmitjana, "The PARIS concept: An experimental demonstration of sea surface altimetry using GPS reflected signals," *IEEE Trans. Geosci. Remote Sens.*, vol. 39, no. 1, pp. 142–150, Jan. 2001.

[11] G. Ruffini, F. Soulat, M. Caparrini, O. Germain, and M. Martin-Neira, "The Eddy experiment: Accurate GNSS-R ocean altimetry from low altitude aircraft," *Geophys. Res. Lett.*, vol. 31, p. L12 306, Jun. 2004.

[12] A. Rius, E. Cardellach, and M. Martin-Neira, "Altimetric analysis of the sea-surface GPS-reflected signals," *IEEE Trans. Geosci. Remote Sens.*, vol. 48, no. 4, pp. 2119–2127, Apr. 2010.

[13] C. Zuffada, A. Fung, J. Parker, M. Okolicanyi, and E. Huang, "Polarization properties of the GPS signal scattered off a wind-driven ocean," *IEEE Trans. Antennas Propag.*, vol. 52, no. 1, pp. 172–187, Jan. 2004.

[14] G. Valenzuela, "Theories for the interaction of electromagnetic and oceanic waves—A review," *Bound.-Layer Meteorol.*, vol. 13, pp. 61–85, Jan. 1978.

[15] P. Beckmann and A. Spizzichino, *The Scattering of Electromagnetic Waves From Rough Surfaces*. New York: Macmillan, 1963.

[16] F. Bass and I. Fuks, *Wave Scattering From Statistically Rough Surfaces*. New York: Pergamon, 1979.

[17] F. Ulaby, R. Moore, and A. Fung, *Microwave Remote Sensing, Active and Passive. Vol. II: Radar Remote Sensing and Surface Scattering and Emission Theory*. Reading, MA: Addison-Wesley, 1982.

[18] J. Stratton, *Electromagnetic Theory*. New York: McGraw-Hill, 1941.

[19] T. Elfouhaily, B. Chapron, K. Katsaros, and D. Vandemark, "A unified directional spectrum for long and short wind-driven waves," *J. Geophys. Res.*, vol. 102, no. C7, pp. 15 781–15 796, Jul. 1997.

Maria Paola Clarizia (S'08) was born in Naples in 1983. She received the M.S. degree in telecommunications engineering (*summa cum laude*) from the University of Sannio, Benevento, Italy, in 2007. She is currently working toward the Ph.D. degree in Global Navigation Satellite System Reflectometry (GNSS-R) in the School of Ocean and Earth Science, National Oceanography Centre, Southampton, U.K.

She is also with the Department of Engineering, University of Sannio. Her current research includes GNSS-R data processing, sea surface simulations, and bistatic signal scattering.

Christine Gommenginger received the Diplôme d'Etudes Approfondies in electromagnetics, telecommunications, and remote sensing from the Université de Toulon et du Var/Université de Nice-Sophia Antipolis, Nice, France, and the Ph.D. degree in microwave radar remote sensing of ocean surface roughness at low grazing angles from the University of Southampton, Southampton, U.K.

She has been with the National Oceanography Centre, Southampton, for over 15 years. Her interests are wide-ranging and include active and passive microwave remote sensing of the ocean, understanding interactions of microwave signals with the ocean surface, remote sensing of ocean wind and waves, and new Earth observation technologies. Her recent work includes research in along-track interferometric synthetic aperture radar (SAR), Global Navigation Satellite System Reflectometry, SAR altimetry, salinity from space, and wide-swath ocean altimetry.

Maurizio Di Bisceglie (M'01) received the Dr.Eng. degree in electronic engineering and the Ph.D. degree in electronics and telecommunications from Università degli Studi di Napoli "Federico II," Naples, Italy.

He has been Research Fellow with the and with the University College of London, London, U.K., and is currently an Associate Professor of telecommunications with University of Sannio, Benevento, Italy. His research activities are in the field of statistical signal processing with applications to radar and remote sensing. He was Organizer of the Italian phase of the European AQUA Thermodynamic Experiment (EAQUATE) mission and the Scientific Director of Mediterranean Agency for Remote Sensing and Environmental Control.

Dr. Di Bisceglie was Cochair of the National Aeronautics and Space Administration Direct Readout Conference in 2005.

Carmela Galdi (M'01) received the Dr.Eng. and Ph.D. degrees in electronic engineering from Università degli Studi di Napoli "Federico II," Naples, Italy, in 1992 and 1997, respectively.

During 1993, she was a Software Engineer with Alcatel Italia, Salerno, Italy. She has been with Università degli Studi di Napoli "Federico II" from 1994 to 2000, and in 2000, she joined the University of Sannio, Benevento, Italy, where she is currently a Professor of telecommunications. In 1995, she spent a four-month period for study and research in the Signal Processing Division, University of Strathclyde, Glasgow, U.K. She was a Visiting Scientist at the University College of London, London, U.K., and at the Defence Evaluation and Research Agency, Malvern, U.K. Her research interests are in the field of statistical signal processing, non-Gaussian models of radar backscattering, and remote sensing applications.

Dr. Galdi was in the organizing committee of the IEEE 2008 Radar Conference.

Meric A. Srokosz received the B.Sc. and Ph.D. degrees in mathematics from Bristol University, Bristol, U.K., in 1976 and 1980, respectively.

He has been a Principal Investigator or Coinvestigator on a number of Earth observation missions, including the European Space Agency (ESA)'s ERS-1, ERS-2, and Envisat missions, the National Aeronautics and Space Administration/Centre National d'Études Spatiales Topex/Poseidon and Jason missions, the National Space Development Agency ADEOS and TRMM missions, and most recently, the ESA SMOS mission. Since 2001, he has been the Scientific Coordinator of the U.K. Natural Environment Research Council's Rapid Climate Change (RAPID) program. He is part of the Marine Physics and Ocean Climate Group, National Oceanography Centre, Southampton, U.K. He has over 30 years of experience in the fields of applied mathematics, wave studies, and remote sensing of the oceans. His research interests include rain from altimetry, plankton patchiness using ship and satellite sensors, data assimilation into biological models, altimeter sea-state bias, breaking waves, salinity from space, and sea surface temperature from passive microwave.